Islamic Azad University

Journal of

Optoelectronical Nanostructures

Spring 2021 / Vol. 6, No. 2

Study of the Spin-Orbit Interaction Effects on Energy Levels and the Absorption Coefficients of Spherical Quantum Dot and Quantum Anti-Dot under the Magnetic Field

Fatemeh Rahimi[1], Tooraj Ghaffary[*,1], Yaghoob Naimi[2], Hadi Khajehazad[1]

[1] Department of Physics, Faculty of Sciences, Shiraz Branch, Islamic Azad University, Shiraz, Iran

[2] Department of Physics, Lamerd Higher Education Center, Lamerd, Iran

(Received 28 Apr. 2021; Revised 24 May 2021; Accepted 29 May 2021; Published 15 Jun. 2021)

Abstract: In this study, the energy levels of spherical quantum dot (QD) and spherical quantum anti-dot (QAD) with hydrogenic impurity in the center, in the presence of spin-orbit interaction (SOI) and weak external magnetic field have been studied. To this aim, solving the Schrodinger equation for the discussed systems by using the finite difference method, the wave functions and energies of these systems are calculated. Then the effect of the external magnetic field, system radius size and height of potential barrier on the energy levels and also the linear, nonlinear and total absorption coefficients, (ACs), of the mentioned systems are studied. Numerical results show that the SOI in both models causes a split of $2p$ level into two sub-levels of $2p_{1/2}$and $2p_{3/2}$ where the low index indicates the total angular momentum J. Also, considering the electron spin, under an applied magnetic field, The $1s$ and $2p$ levels split into two sub-levels and six sub-levels, respectively. Furthermore, in this research, it is proved that energy changes are significantly different as a function of radius size and height of the potential barrier in QD and QAD models and the ACs of these systems behave differently according to the incident photon energy at the same condition.

Keywords: Quantum Dot, Quantum Anti-Dot, Confinement Potential, Spin-Orbit Interaction, Magnetic Field, Absorption Coefficient.

[*] Corresponding author. Email: **tooraj.gh@gmail.com**

1. INTRODUCTION

Recent advances in nanomaterial production technologies have led to a wide range of studies based on the electronic structures and optical properties of semiconductor QDs and QADs [1-10]. Quantum confinements in these structures completely quantized their energy levels and consequently change their physical properties. Therefore, considerable research on the effect of radius size, the effects of external electric and magnetic fields and control parameters such as temperature and hydrostatic pressure on the physical properties of these nanostructures, have been done experimentally and theoretically. [11-19]

Moreover, electron spin plays an important role in the electronic structure of the nanostructures in question and can significantly affect their physical properties. It is fully known that the SOI and spin-related phenomena are major issues in low-dimensional structures, because spin is the key ingredient in the emerging field of spintronics [20-28].

The conventional SOI, which occurs naturally and also is predicted in Dirac's theory of relativity, exists for excited states such as 2p, 3d, and 4f in a spherical QDs (QADs). Generally, SOI is due to the interaction between spin and orbital motion of the donor electron, which is given by the familiar Hamiltonian Eq. (6). As the principles of quantum mechanics express is due to electron motion in an electrostatic field [29-31]. Such an interaction splits up the degeneracy associated with the J quantum number (total angular momentum) even in the absence of a magnetic field. In addition, considering the electron spin causes each energy level to split into $2 \times (2l + 1)$ sub-levels in the presence of an external magnetic field, sometimes called the anomalous Zeeman effect, where l is the quantum number of the angular momentum. [29,30].

In this study, the energy changes of 2p level of spherical $GaAs/Ga_{1-x}Al_xAs$ ($Ga_{1-x}Al_xAs/GaAs$) QDs (QADs) considering the SOI that determines the fine structure of the nanostructures in question are investigated. Furthermore, by applying an external magnetic field in the presence of SOI, the Zeeman splitting of 1s and 2p levels are defined and then the energy changes of these levels are studied according to the changes in core radius, total radius and height of the potential barrier. Eventually, the ACs of these systems have been discussed.

2. THE HAMILTONIAN AND PHYSICAL MODEL

In this paper, two models of spherical $GaAs/Ga_{1-x}Al_xAs$ QD and spherical $Ga_{1-x}Al_xAs/GaAs$ QAD with hydrogenic impurity in the center are investigated when the electron is bounded by a finite potential barrier. This study is performed considering the SOI in the presence of an external magnetic field. The Hamiltonian of an electron with the above conditions is given as follows when a uniform magnetic field is applied along the Z-axis [30].

$$H = H_0 + H_B + H_{SO} \tag{1}$$

H_0 is the Hamiltonian without SOI and magnetic field. H_B refers to the Hamiltonian related to the magnetic field and H_{SO} is the SOI Hamiltonian.

The calculations will be performed in the Rydberg unit. So for H_0 we have [12]:

$$H_0 = -\nabla^2 - \frac{2}{r} + V_C(r) \tag{2}$$

$V_C(r)$ is the confinement potential and it has the following form for $GaAs/Ga_{1-x}Al_xAs$ QD:

$$V_C^{QD}(r) = \begin{cases} V_0 & r \le R_1 \\ V_1 & R_1 < R \le R_2 \\ \infty & otherwise \end{cases} \tag{3}$$

where V_0 and V_1 are confinement potential height (see fig. 1).

Rearranging the layers, the confinement potential for constructing $Ga_{1-x}Al_xAs/GaAs$ QAD is defined as follows:

$$V_C^{QAD}(r) = \begin{cases} V_1 & r \le R_1 \\ V_0 & R_1 < R \le R_2 \\ \infty & otherwise \end{cases} \tag{4}$$

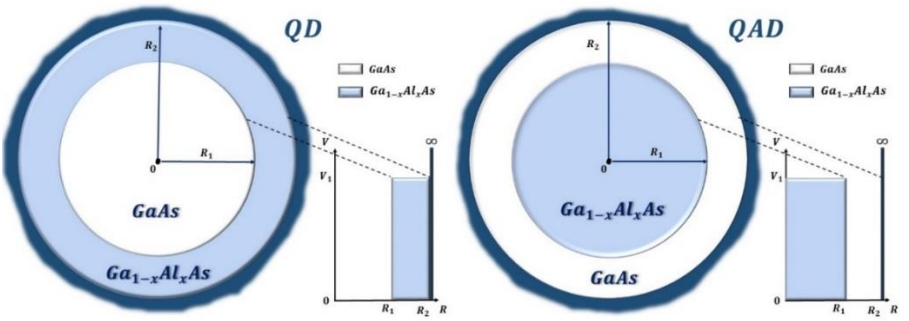

Fig. 1. Geometrical and potential energy scheme of QD and QAD. R_1 is the core radius, R_2 is the total radius

H_B in the Eq. (1) is given by:

$$H_B = \frac{1}{4}\gamma^2 r^2 sin^2\theta + m\gamma + \frac{1}{2}g\gamma\sigma_z \tag{5}$$

The γ-term is the dimensionless quantity to control the magnetic field strength and defined by $\gamma = a_0^{*2} eB/\hbar$, (where $a_0^* = 4\pi\varepsilon\hbar^2/m^* e^2$ is the effective Bohr radius). The parameters e, m^* and ε are the electron charge, the effective mass of the electron and the dielectric constant, respectively. m is the azimuthal quantum numbers and $Ry^* = m^* e^4/32\pi^2\varepsilon^2\hbar^2$ is the unit of energy. θ is the angle between r and z axis, g is the Landé factor and $\frac{1}{2}\sigma_z$ is the z projection of electron spin with $\sigma_z = \pm 1$. Here, $\sigma_z = +1$ represents spin up and $\sigma_z = -1$ represents spin down.

H_{SO} in the Eq. (1) expressed by [28-31]:

$$H_{SO} = \xi(r)\vec{L}.\vec{S} \tag{6}$$

where

$$\xi(r) = \frac{1}{2m^{*2}c^2 r}\frac{d}{dr}\phi(r)\left(\vec{L}.\vec{S}\right) \tag{7}$$

where S is the spin vector of electron. $\vec{L}.\vec{S} = \frac{\hbar^2}{2}[J(J+1) - l(l+1) - S(S+1)]$ and $J = l \pm S$ is the total angular momentum.

Considering the Coulomb potential $\phi(r) = \frac{-e^2}{4\pi\varepsilon_0\varepsilon_r r}$, H_{SO} in the Rydberg unit is simplified as follows:

$$H_{SO} = \frac{4}{c^2 r^3}\left(\vec{L}.\vec{S}\right) \tag{8}$$

According to Eq. (8), the splitting due to SOI should be approximately in order of $\frac{4}{c^2 a^{*3}} \sim 10^{-5}\ (Ry^*)$.

Considering Eqs. (2), (5) and (8), the Hamiltonian in Eq. (1) in the Rydberg unit is obtained as follows:

$$\xi = \frac{1}{r^2}\frac{\partial}{\partial r}\left(r^2\frac{\partial}{\partial r}\right) + \frac{l(l+1)}{r^2} + \frac{1}{4}\gamma^2 r^2 sin^2\theta + m\gamma - \frac{2}{r} + \frac{4}{c^2 r^3}\left(\vec{L}.\vec{S}\right) + \frac{1}{2}g\gamma\sigma_z + V_C(r) \tag{9}$$

where l is the angular momentum quantum number. If H_B is assumed to be very weak, then H_{SO} is much more important than H_B, and H_B can be considered as a small disturbance. The eigenvalue equation for the main Hamilton $H^0 = H_0 + H_{SO}$ is defined as follows:

$$\xi H^0 \psi_{nlm}^{(0)}(r,\theta,\varphi) = E_{nl}^{(0)}\psi_{nlm}^{(0)}(r,\theta,\varphi) \tag{10}$$

where $\psi_{nlm}^{(0)}(r,\theta,\varphi)$ is the wave function of H^0 and n is the principal quantum number.

$\psi_{nlm}^{(0)}(r,\theta,\varphi)$ in Eq. (8) can be written as:

$$\psi_{nlm}^{(0)}(r,\theta,\varphi) = R_{nl}^{(0)}(r)Y_{lm}(\theta,\varphi) \tag{11}$$

where $R_{nl}^{(0)}(r)$ and $Y_{lm}(\theta,\varphi)$ are the radial and the angular wave function of H^0respectively.

The total H- wave function can be extended as below:

$$\psi(r,\theta,\varphi) = \sum_j C_j \psi_j^{(0)}(r,\theta,\varphi) \tag{12}$$

here

$$\psi_j^{(0)}(r,\theta,\varphi) = R_{n_j l_j}^{(0)}(r)Y_{l_j m_j}(\theta,\varphi) \tag{13}$$

is the j-th wave function of the H^0.

Matrix elements of the total Hamiltonian of the system according to above bases can be written as:

$$H_{ij} = \langle \psi_i | H^0 + H^I | \psi_j \rangle = E_{ij}^0 \delta_{ij} + H_{ij}^I \tag{14}$$

where $H^I = H_B$ is the perturbed Hamiltonian and:

$$H_{ij}^I = \int_0^{R_2} Y_{l_i m_i}^*(\theta, \varphi) R_{n_i l_i}^{(0)}(r) H^I R_{n_j l_j}^{(0)}(r)\, Y_{l_j m_j}(\theta, \varphi) \tag{15}$$

By diagonalizing the generated Hamiltonian matrix, energy levels and corresponding wave functions can be obtained, and according to the magnitude of the applied magnetic field and different confinement potentials, one can also measure changes in energy levels and study the optical properties.

3. ABSORPTION COEFFICIENTS

By using the density matrix formalism, the optical properties for the discussed systems can be calculated. Considering the intersubband transitions of a spherical QD(QAD), we suppose that the system is excited by an incident light as,

$$E(t) = \tilde{E} e^{i\omega t} + \tilde{E} e^{-i\omega t} \tag{16}$$

E is the vertical electromagnetic field along the *z* axis. The Hamiltonian of system is written as follows

$$H' = H + ezE(t) \tag{17}$$

where *H* is the Hamiltonian of system without the electromagnetic field *E(t)*. The total AC can be expressed as [32,33]

$$\alpha(\omega, I) = \alpha^{(1)}(\omega) + \alpha^{(3)}(\omega, I) \tag{18}$$

where

$$\alpha^{(1)}(\omega) = \sqrt{\frac{\mu}{\varepsilon_R}} \frac{\sigma_v \hbar\omega \Gamma_{fi} |M_{fi}|^2}{\left(E_{fi} - \hbar\omega\right)^2 + \left(\hbar\Gamma_{fi}\right)^2} \tag{19}$$

and

$$\alpha^{(3)}(\omega, I) = -\sqrt{\frac{\mu}{\varepsilon_R}} \left(\frac{I}{2\varepsilon_0 n_r c}\right) \frac{4\sigma_v \hbar\omega \Gamma_{fi} |M_{fi}|^4}{\left[\left(E_{fi} - \hbar\omega\right)^2 + \left(\hbar\Gamma_{fi}\right)^2\right]^2} \tag{20}$$

are the linear and third order nonlinear ACs, respectively and μ, σ_v and n_r are the permeability, carrier density and refractive index of the system respectively. ω is the incident photon energy, $\Gamma_{fi} = \frac{1}{T_{fi}}$, T_{fi} is the relaxing time between initial state and final state (in this work, from ground state 1s to excited state 2p), I is the optical intensity of incident wave and c is the speed of light in the free space. The remained quantities are defined as

$$E_{fi} = E_f - E_i$$

$$\varepsilon_R = n_r^2 \varepsilon_0 \tag{21}$$

$$M_{fi} = \left|\langle \psi_f | ez | \psi_i \rangle\right|$$

where M_{fi} is an element of electric dipole moment matrix that in the spherical coordinate is $\left|\langle \psi_f | er\cos\theta\, | \psi_i \rangle\right|$.

4. NUMERICAL RESULTS AND DISCUSSIONS

In this section, our numerical results for spherical QD and QAD are presented. The constant values that are used in our numerical calculations are: the effective mass of an electron consider as $m^* = 0.067 m_0$ (with $m_0 = 9.10596 \times 10^{-31}$ kg) and the dielectric constant is $\varepsilon = 13.18\varepsilon_0$, hence the effective Bohr radius will be $a_0^* = 10.4nm$ and the effective Rydberg energy is $Ry^* = 5.2meV$. The barrier potential $V_0 = 0$, $V_1 = Q_C 1.247x\ eV$ ($V_1 = Q_C 239.81 x Ry^*$) for the Al concentration x, where $Q_C = 0.6$ is the conduction band offset parameter. The value of the rest of parameters are $\Gamma_{21} = 0.2ps, \sigma_v = 3.0 \times 10^{22}, n_r = 3.2$.

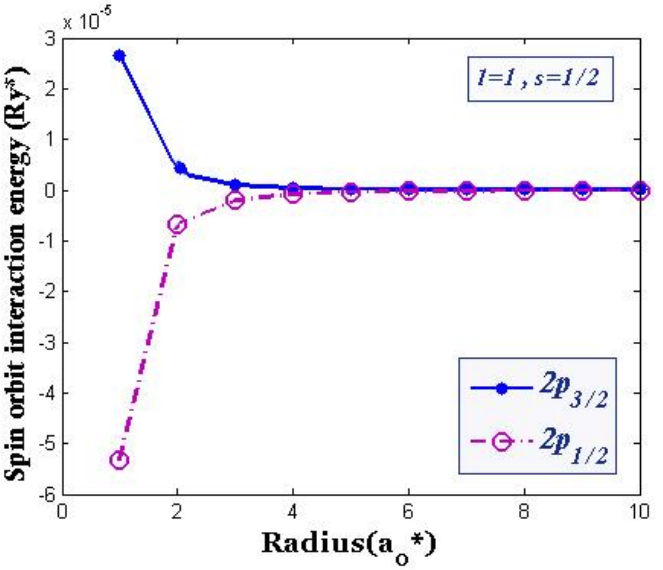

Fig. 2. Energy changes in SOI for $2P$ level as function of radius size

The behavior of SOI for $2p_{1/2}$ and $2p_{3/2}$ levels as a function of radius size is illustrated in Fig. 2. This figure shows that the effect of SOI causes the $2p$ level to be split into two sub-levels $2p_{1/2}$ and $2p_{3/2}$, in which the lower index indicates J. As it can be observed in Fig.2, the splitting vanishes for radii larger than about $R{\sim}5a_0^* = 52nm$ and the energy levels become degenerate again.

Variation of $1s$-energy as a function of γ considering the electron spin, for core radius $R_1 = 1a_0^*$, and total radius $R_2 = 2a_0^*$ for the QD and QAD models are shown in Fig. 3 (a) and (b), respectively. The SOI has no effect on the 1s level and therefore there is no splitting due to the SOI at this level. However, under the applied magnetic field, the electron spin interacts with the magnetic field and this interaction causes this level to be split into two sub-levels, one related to $m_s = \frac{1}{2}, (\sigma = 1)$, and the other related to $m_s = -\frac{1}{2}, (\sigma = -1)$. As can be seen in Fig. 3, applying a weak magnetic field (γ of the order of 10^{-4}), and due to the interaction of the spin and magnetic field, $1s$ level is split into two sub-levels $(m = 0, \sigma_z = 1)$ and $(m = 0, \sigma_z = -1)$ that the amount of these splitting for both QD and QAD models is at the order of $10^{-4}Ry^*$.

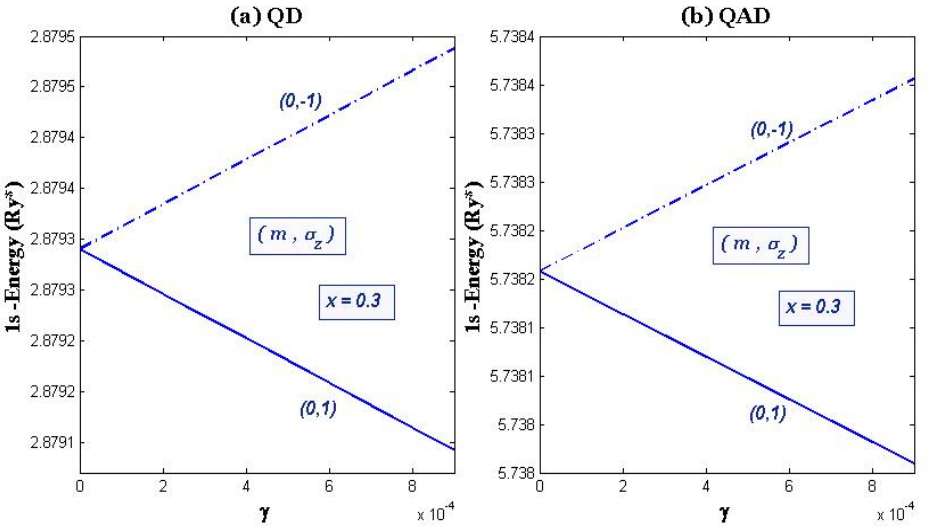

Fig. 3 $1s$-energy level as a function of γ, with $R_1 = 1a_0^*$, $R_2 = 2a_0^*$ and $x = 0.3$

Fig. 4 shows the behavior of the 2p energy level, as a function of γ considering the electron spin for core radius $R_1 = 1a_0^*$, and total radius $R_2 = 2a_0^*$. The SOI splits the 2P state energy level into two sub-levels $2p_{1/2}$ and $2p_{3/2}$. On the other hand, under the applied magnetic field, the electron spin interacts with the magnetic field, and this interaction causes energy levels to be split into $2(2l + 1)$ sub-levels. Therefore, the $2p$ state energy level $(n = 2\,, l = 1\,,\ m = -1,0,1\,)$ is split into six sub-levels with, $(m = 0, \sigma_z = 1)$, $(m = 0, \sigma_z = -1)$, $(m = 1, \sigma_z = 1)$, $(m = 1, \sigma_z = -1)$, $(m = -1, \sigma_z = 1)$and $(m = -1, \sigma_z = -1)$. In Fig. 4 the splitting of the levels are clearly visible. The rate of these splitting for both QD and QAD models are at the order of $10^{-4} Ry^*$.

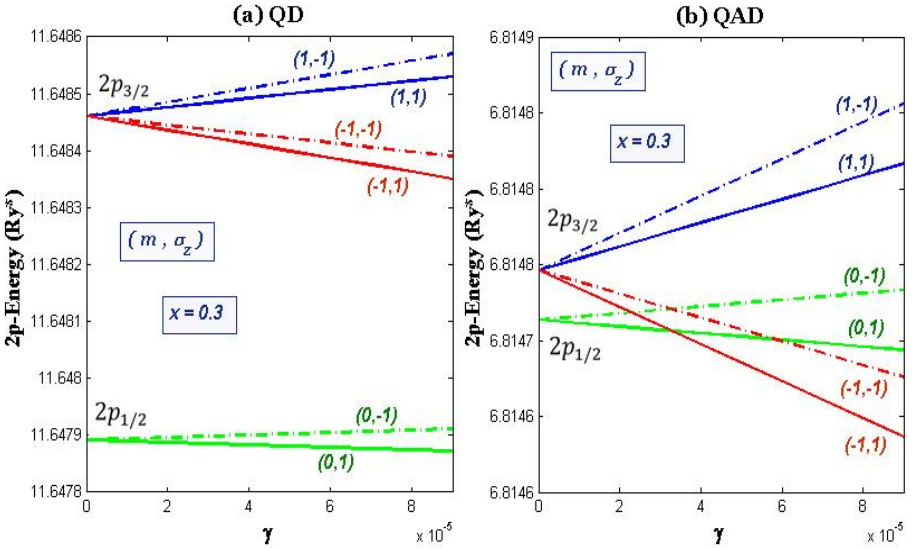

Fig. 4 $2p$-energy level as a function of γ, with $R_1 = 1a_0^*$, $R_2 = 2a_0^*$ and $x = 0.3$

The effect of core radius R_1, on the 1s and 2p energies of QD and QAD for total radius $R_2 = 2a_0^*$ at $\gamma = 3 \times 10^{-4}$ is presented in Fig. 5 (a) and (b), respectively. From Fig. 5, it is clear that these two models have the opposite behavior as a function of the core radius. The energy levels of QD decrease with increasing R_1 and in larger radii, the energies tend to remain constant. However, the energy levels of the QAD increase with increasing R_1. These behaviors correspond to the correlation between energy and system size parameters (i.e. energy is proportional to well width). At the QD model, $E \propto \frac{1}{R_1}$, while at the QAD model, $E \propto \frac{1}{R_2 - R_1}$, therefore, as R_1 increases, the energies decrease for QD model and increases for QAD model. Fig. 5 is also magnified in the indicated ranges to determine the Zeeman splitting between the energy levels. It can be seen that, as expected, the 1s level is split into two sub-levels and the 2p level is split into six sub-levels.

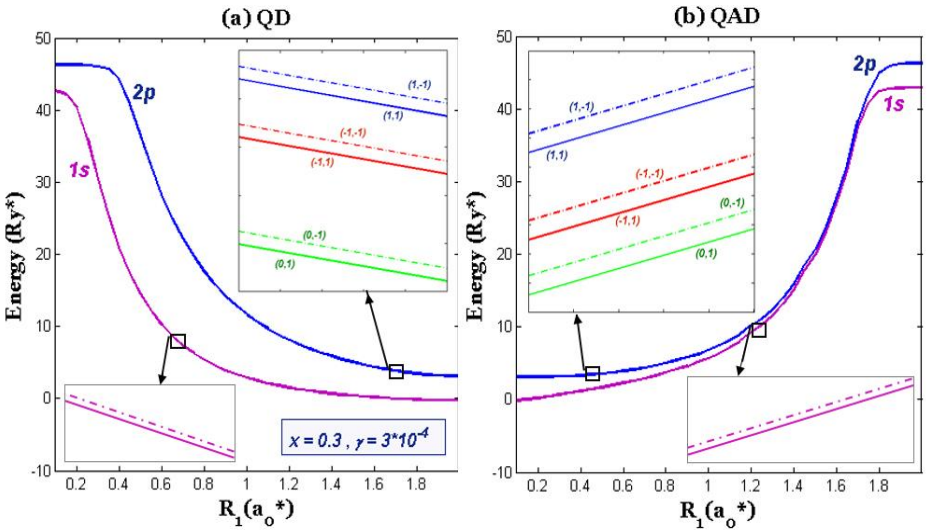

Fig. 5. 1s and $2p$-energy levels as a function of R_1 with $R_2 = 2a_0^*$, x =0.3 and $\gamma = 3 \times 10^{-4}$

The sensitively of 1s and $2p$ energies as a function of R_2 for core radius $R_1 = 1a_0^*$ at $\gamma = 3 \times 10^{-4}$ are illustrated in Fig. 6. According to this figure with increasing R_2, the energies of both QD and QAD models are reduced. In the QD model, increasing R_2 leads to a greater barrier thickness. Electrons tunnel into the barrier, their energies decrease and reach constant values at large R_2. In the QAD model, when R_2 increases, the width of the well actually increases, and so the energies decrease. Fig. 6 is also magnified in the specified ranges to determine the Zeeman splitting between the energy levels. As can be seen, the 1s level is split into two sub-levels and the 2p level is split into six sub-levels.

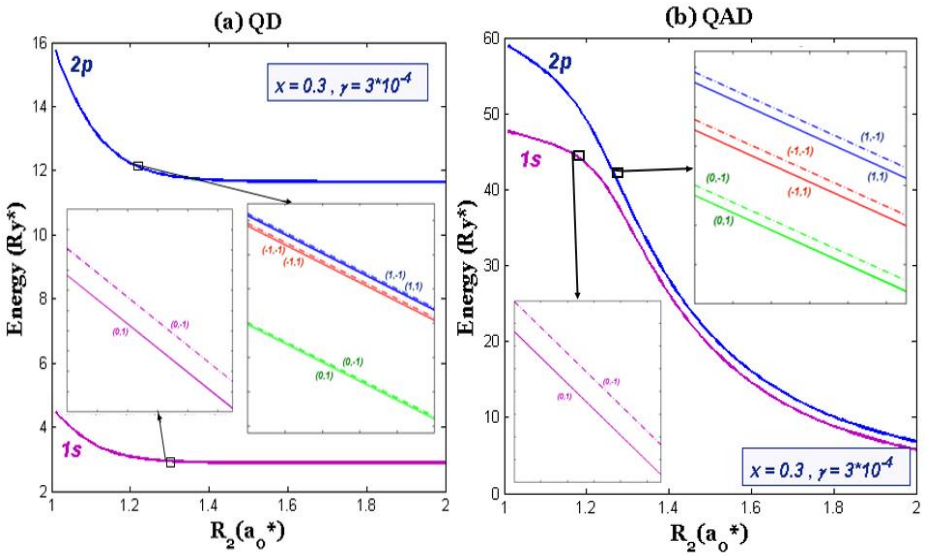

Fig. 6. 1s and $2p$-energy levels as a function of R_2, with $R_1 = 1a_0^*$, x =0.3 and $\gamma = 3 \times 10^{-4}$

In Fig. 7, the results for the 1s and 2p-energeis as a function of *Al* concentration x are depicted at $\gamma = 3 \times 10^{-4}$ for (a) QD model and (b) QAD model. By changing x from 0 to 1, the height of barrier changes from 0 to $144Ry*$. As can be seen in Fig. 7, in both models the energies increase by increasing x. Moreover, diagrams are magnified within the indicated ranges to indicate the Zeeman splitting between the energy levels. It can be seen that the 1s level is split into two sub-levels and the 2p level is split into six sub-levels.

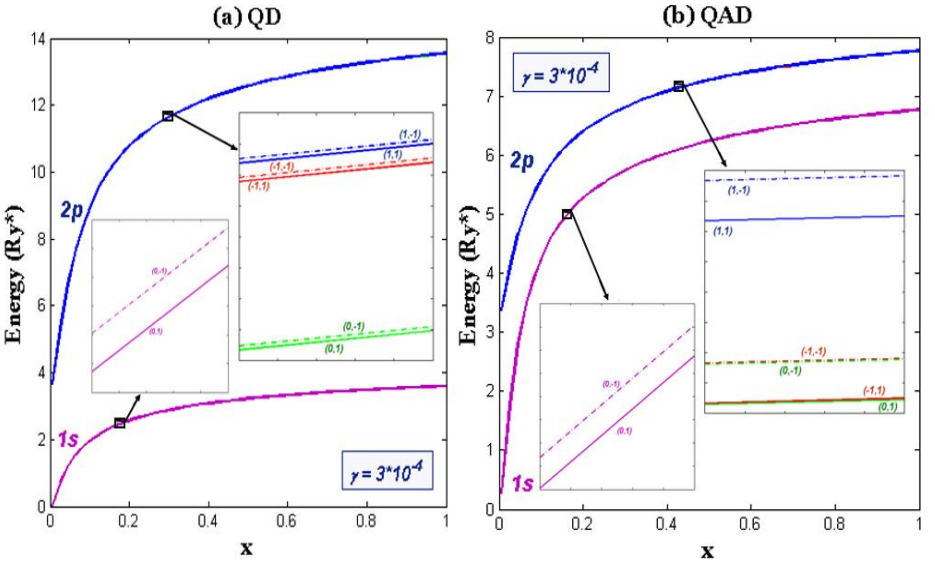

Fig. 7. 1s and $2p$-energy levels as a function of x, with $R_1 = 1a_0^*$, $R_2 = 2a_0^*$ and $\gamma = 3 \times 10^{-4}$

In Fig. 8 the linear, nonlinear and total ACs as a function of incident photon energy for $1s_{1/2} \rightarrow 2p_{1/2}$ in the same conditions are plotted. From Fig.8, it is clear that the ACs of the QD and QAD have different performances with respect to incident photon energy in the same condition. In the case of comparing the total AC curves, this figure shows that the QD has an approximately symmetric curve but QAD has a curve that abruptly increases then asymptotically goes to zero. In the case of the nonlinear AC curves, it is obvious that for this selected intensity value, the QD has no significant nonlinear AC but the QAD shows a significant nonlinear AC.

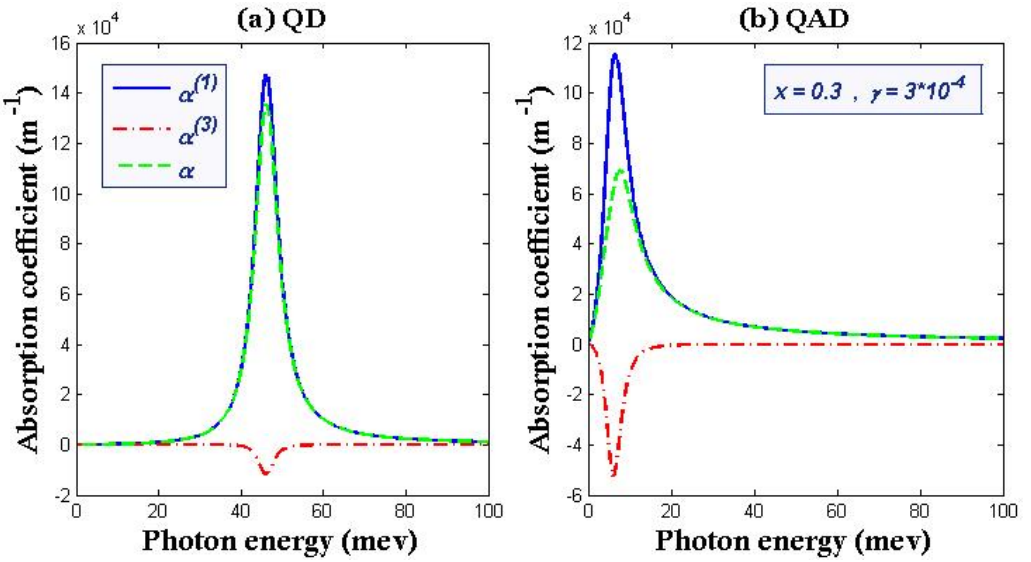

Fig. 8 The linear, nonlinear and total ACs as a function of incident photon energy with $I = 300MW/m^2$, $R_1 = 1a_0^*$, $R_2 = 2a_0^*$,x= 0.3 and $\gamma = 3 \times 10^{-4}$

Fig. 9 shows the linear, nonlinear and total $1s_{1/2} \rightarrow 2p_{1/2}$ absorption coefficients as a function of the photon energy for (a) QD and (b) QAD. It is observed that as the optical intensity increases, the total AC decreases for both QD and QAD. This is because the nonlinear absorption (which is negative) enhances with an increase in intensity. In Fig. 9(b) the behavior of QAD has been shown for total ACs curves, which magnitude of the intensity value goes from $I = 100MW/m^2$ to $500MW/m^2$ at fixed incremental steps of $100MW/m^2$. If this range of intensity is used for the QD, the change of nonlinear AC and therefore in the total AC for QD is small, so we used the range $100 \leq I \leq 900$ with the fixed incremental steps of $200MW/m^2$ in Fig.9 (a). In these two figures the highest curve corresponds to the highest intensity, and the downward ones correspond to the lower intensities, respectively.

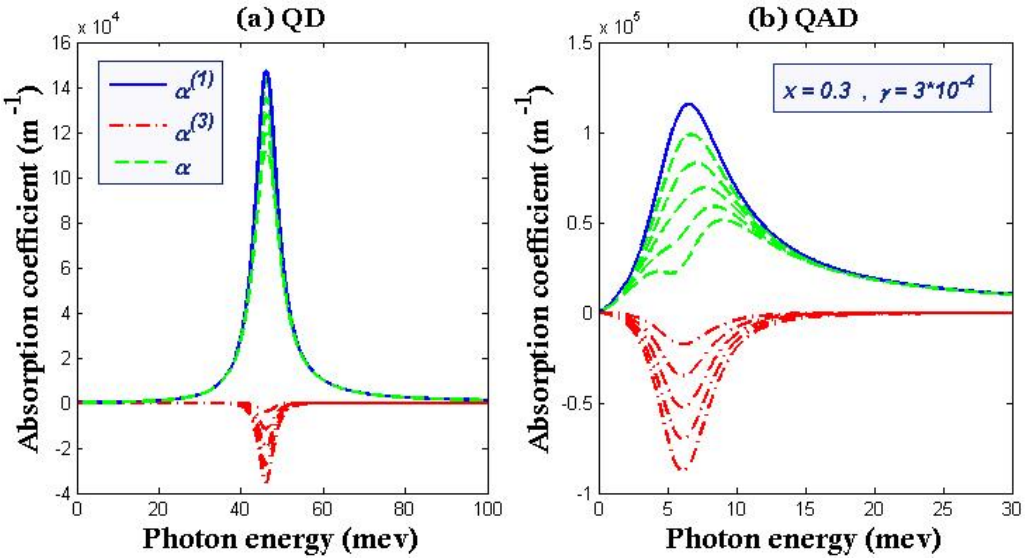

Fig. 9 The linear, nonlinear and total ACs as a function of incident photon energy with $R_1 = 1a_0^*$, $R_2 = 2a_0^*$, x= 0.3 and $\gamma = 3 \times 10^{-4}$ and five different intensities for (a) QD and (b) QAD. The solid lines show linear absorption coefficients. The dash-dotted lines are nonlinear absorption coefficient curves and dashed lines represent the total absorption coefficient curves.

In Fig. 10, the total $1s_{1/2} \rightarrow 2p_{1/2}$ AC for both QD and QAD as a function of incident photon energy for four different core radius are plotted. Fig. 10(a) shows that as the core radius increases, the total AC peak heights remain almost constant but move toward a smaller incident photon energies. However, Fig. 10(b) shows that by increasing the amount of core radius, the total AC peak heights become larger and slightly shift toward lower incident photon energies. The reasons for these behaviors are that in the case of the QD model, increasing the core radius reduces the quantum constraint. Thus, the energy differences between the sub-levels decreases and the peaks shift to lower energies. Conversely, in the QAD model, increasing the core radius increases the quantum constraint. Thus, the energy differences between the sub-levels increases and the peaks shift to higher energies.

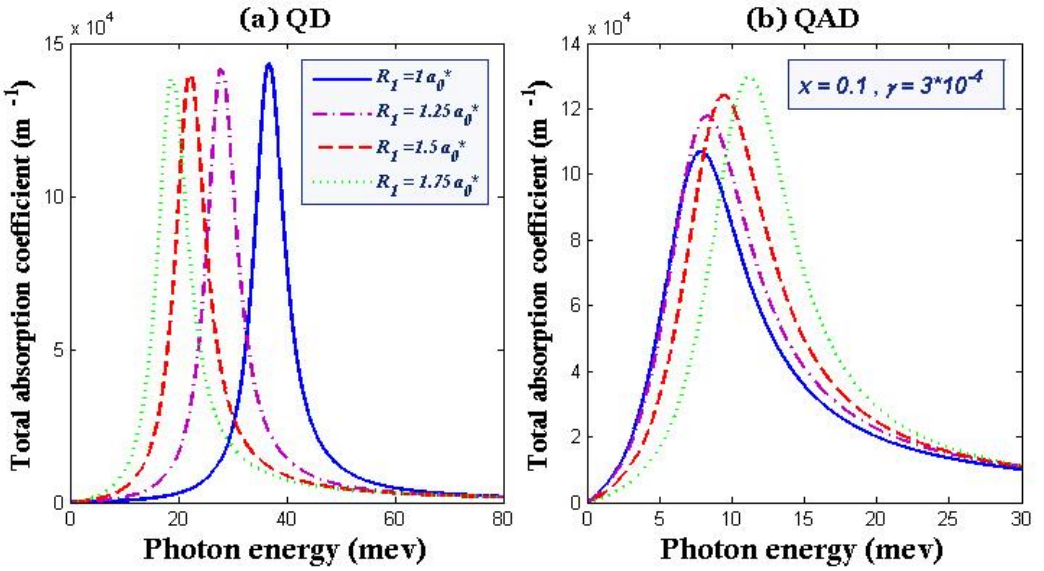

Fig. 10 The total ACs as a function of incident photon energy with $I = 100MW/m^2$, $R_2 = 2a_0^*$, x= 0.3 and $\gamma = 3 \times 10^{-4}$ and four different core radius.

5. CONCLUSION

In this study, the effect of a weak external magnetic field on the 1s and 2p energy levels of the spherical $GaAs/Ga_{1-x}Al_xAs$ QD and spherical $Ga_{1-x}Al_xAs/GaAs$ QAD models in the presence of SOI have been investigated. The results show that the interaction between the spin and the external magnetic field causes the 1s level to be split into two sub-levels. Also, for both models, the SOI splits the 2P level into two sub-levels, $2p_{1/2}$ and $2p_{3/2}$. On the other hand, considering the electron spin, the presence of an external magnetic field causes the 2P level to be split into six sublevels. It has been shown that the QD model has a different behavior compare to the QAD model regarding energy changes as function of system radius size and height of the potential barrier. Furthermore, the ACs of these systems have been discussed and shows that the ACs of the QD and QAD have different performances with respect to incident photon energy in the same condition.

REFERENCES

[1] K.A. Rodríguez-Magdaleno, R. Pérez-Álvarez, J.C. Martínez-Orozco, Intra-miniband absorption coefficient in $GaAs/Al_xGa_{1-x}As$ core/shell spherical quantum dot, Journal of Alloys and Compounds. 736 (2018) 211–215.

[2] M. Servatkhah, Study of RbCl quantum pseudo-dot qubits using Shannon and Laplace entropies, Optical and Quantum Electronics. 52 (2020) 126.

[3] Y. Naimi, J. Vahedi, M. R. Soltani, Effect of position-dependent effective mass on optical properties of spherical nanostructures, Optical and Quantum Electronics. 47 (2015) 2947-2956.

[4] F. Hakimian, M.R. Shayesteh, M.R. Moslemi, Proposal for Modeling of FWM Efficiency of QD-SOA Based on the Pump/Probe Measurement Technique, journal of optoelectronical nanostructures. 5 (4) (2020) 49-65.

[5] M. R. Mohebbifar, Study of the Quantum Efficiency of Semiconductor Quantum Dot Pulsed Micro-Laser, journal of optoelectronical nanostructures. 6 (1) (2021) 59-69.

[6] M. Servatkhah, R. Pourmand, Optical properties of a two-dimensional GaAs quantum dot under strain and magnetic field, The European Physical Journal Plus.135 (2020) 754.

[7] M. Rezvani Jalal, M. Habibi, Simulation of Direct Pumping of Quantum Dots in a Quantum Dot Laser, journal of optoelectronical nanostructures. 2 (2) (2017) 61-69.

[8] E.B. Al, E. Kasapoglu, H. Sari, I. Sökmen, Optical properties of spherical quantum dot in the presence of donor impurity under the magnetic field, Physica B. 613 (2021) 412874.

[9] L. Stevanović, N. Filipović, V. Pavlović, Effect of magnetic field on absorption coefficients, refractive index changes and group index of spherical quantum dot with hydrogenic impurity, Journal of Luminescence, Optical Materials. 91 (2019) 62–69.

[10] F. Rahmani, J. Hasanzadeh, Investigation of the Third-Order Nonlinear Optical Susceptibilities and Nonlinear Refractive Index In Pbs/Cdse/Cds Spherical Quantum Dot, journal of optoelectronical nanostructures. 3 (1) (2018) 65-78.

[11] G.V.B. de Souza, A. Bruno-Alfonso, Finite-difference calculation of donor energy levels in a spherical quantum dot subject to a magnetic field, Physica E. 66 (2015) 128–132.

[12] E.B. Al, E. Kasapoglu, S. Sakiroglu, H. Sari, I. Sokmen, C.A. Duque, Binding energies and optical absorption of donor impurities in spherical quantum dot under applied magnetic field, Physica E. 119 (2020) 114011.

[13] H. Bahramiyan, M. Servatkhah, Second and third harmonic generation of a hexagonal pyramid quantum dot: impurity position effect, Optical and Quantum Electronics. 47 (2015) 2747-2758.

[14] Y. Naimi, Refractive index changes of a donor impurity in spherical nanostructures: Effects of hydrostatic pressure and temperature, Phys. B. 428 (2013) 43–47.

[15] M. R. K. Vahdani, G. Rezaei, Linear and nonlinear optical properties of a hydrogenic donor in lens-shaped quantum dots, Physics Letters A. 373 (2009) 3079–3084.

[16] M. Elamathi, A. John Peter, Exciton radiative recombination time in a group III-V/II-VI core/shell quantum dot: Simultaneous effects of pressure and temperature, Chemical Physics Letters. 770 (2021) 138454.

[17] Y. Naimi, A.R. Jafari, Optical properties of quantum dots versus quantum antidots: Effects of hydrostatic pressure and temperature, Journal of Computational Electronics. 13 (2014) 666-672.

[18] R. Khordad, M. Servatkhah, Study of entanglement entropy and exchange coupling in two-electron coupled quantum dots, Optical and Quantum Electronics. 49 (2017) 217.

[19] H. Bahramiyan lal, S. Bagheri, Linear and nonlinear optical properties of a modified Gaussian quantum dot: pressure, temperature and impurity effect, journal of optoelectronical nanostructures. 3 (3) (2018) 79-100.

[20] R.A. Zak, D.L. Maslov, D. Loss, Spin susceptibility of interacting two-dimensional electrons in the presence of spin-orbit coupling, Physical Review B. 82 (2010) 115415.

[21] H. Hartmann, D. Schuck, Spin-orbit coupling for the motion of a particle in a ring-shaped potential, Int. J. Quant. Chem. 18 (1980) 125-141.

[22] H.K. Sharma, A. Boda, B. Boyacioglu, A. Chatterjee, Electronic and magnetic properties of a two-electron Gaussian GaAs quantum dot with spin-Zeeman term: A study by numerical diagonalization, Journal of Magnetism and Magnetic Materials. 469 (2019) 171–177.

[23] A. Bagga, P. Pietiläinen, T. Chakraborty, Spin hot spots in vertically coupled few-electron isolated quantum dots, Physical Review B. 74 (2006) 033313.

[24] M. Z. Malik, D.S. Kumar, S. Mukhopadhyay, A. Chatterjee, Role of spin-orbit interactions on the entropy and heat capacity of a quantum dot helium placed in an external magnetic field, Physica E. 121 (2020) 114097.

[25] A.L. Vartanian, A.A. Kirakosyan, K.A. Vardanyan, Spin relaxation mediated by spin-orbit and acoustic phonon interactions in a single-electron two-dimensional quantum dot, Superlattices and Microstructures.122 (2018) 548-556.

[26] P. Saini, A. Chatterjee, Confnement shape effect on D^0 impurity in a GaAs quantum dot with spin-orbit coupling in a magnetic field, Superlattices and Microstructures.146 (2020) 106641.

[27] V. Nautiyal, D. Munjal, P. Silotia, Spin orbit effect in a quantum dot confined in a Kratzer potential, Journal of Magnetism and Magnetic Materials. 528 (2021) 167688.

[28] S. Rajashabala, K. Navaneethakrishnan, Pressure effects on the spin–orbit interactions in low-dimensional quantum well systems, Physica E. 40 (2008) 843–848.

[29] S. Gasiorowicz, Quantum Physics. Third Edition Reading. US: Addison Wesley (2003).

[30] J. J. Sakurai, Advanced quantum Mechanics. Reading. MA: Addison-Wesley (1967).

[31] R.S. Daries Bella, K. Navaneethakrishnan, Donor binding energies and spin–orbit coupling in a spherical quantum dot, Solid State Communications. 130 (2004) 773–776.

[32] S. Unlu, I. Karabulut, H. Safak, Linear and nonlinear intersubband optical absorption coefficients and refractive index changes in a quantum box with finite confining potential, Phys. E. 33 (2006) 319–324.

[33] C. Zhang, Z. Wang, M. Gu, Y. Liu, K. Guo, Nonlinear optical absorption coefficients and refractive index changes in a two dimensional system, Phys. B. 405 (2010) 4366–4369.